Truncated Gaussian-Bessel beams for short-pulse processing of small-aspect-ratio micro-channels in dielectrics

Xing Liu, Qingfeng Li, Aurélien Sikora, Marc Sentis, O. Uteza, Razvan Stoian, W Zhao, G Cheng, N. Sanner

Research Article | Vol. 27, No. 5 | 4 Mar 2019 | OPTICS EXPRESS 6996
Optics EXPRESS

Truncated Gaussian-Bessel beams for short-pulse processing of small-aspect-ratio micro-channels in dielectrics

X. Liu,[1,2,3] Q. Li,[3] A. Sikora,[3] M. Sentis,[3] O. Utéza,[3] R. Stoian,[4] W. Zhao,[1] G. Cheng,[1] and N. Sanner[3,*]

[1]*State Key Laboratory of Transient Optics and Photonics, Xi'an Institute of Optics and Precision Mechanics of CAS, Xi'an 710119, China*
[2]*University of Chinese Academy of Sciences, Beijing 100049, China*
[3]*Aix-Marseille University, CNRS, LP3 UMR 7341, F-13288 Marseille, France*
[4]*Laboratoire Hubert Curien, UMR CNRS 5516, Université de Lyon, Université Jean Monnet, 42000 Saint Etienne, France*
**nicolas.sanner@univ-amu.fr*

Abstract: In order to control the length of micro-channels ablated at the surface of dielectrics, we use annular filtering apertures for tailoring the depth of focus of micrometric Gaussian-Bessel beams. We identify experimentally and numerically the appropriate beam truncation that promotes a smooth axial distribution of intensity with a small elongation, suitable for processing micro-channels of small aspect ratio. Single-shot channel fabrication is demonstrated on the front surface of a fused silica sample, with sub-micron diameter, high-quality opening, and depth of few micrometers, using 1 ps low-energy (< 0.45 μJ) pulse. Finally, we realize 10 × 10 matrices of densely packed channels with aspect ratio ~5 and a spatial period down to 1.5 μm, as a prospective demonstration of direct laser fabrication of 2D photonic-crystal structures.

1. Introduction

Bessel beams have attracted great attention since firstly demonstrated by Durnin [1]. Such beams can maintain their transverse shape invariant over quite long propagation distance, denoted as "diffraction-free". Moreover, they have the capability to reconstruct themselves behind a small obstacle, exhibiting high robustness during propagation [2]. These features make Bessel beams attractive in the field of super-resolution imaging [3], optical manipulation [4,5], and laser machining [6–10]. In the context of deep drilling with ultrafast laser pulse in transparent materials, zero-order Bessel beam shows its decisive advantages over Gaussian beam, that can be summarized in terms of penetration geometry, nonlinear robustness and interaction phenomenology [11,12]. In particular, a Bessel beam overcomes to certain extent the transient surface plasma screening effects that limit Gaussian beam applicability to depths of hundreds of nanometers [13], since it permits extended penetration of the laser pulse inside the bulk material. Ultrahigh aspect ratio (depth/diameter) channels exceeding 1200:1 have been reported [14] by using femtosecond (fs) micro-Bessel beams. Juxtaposing several nanochannels has proven its efficiency for cutting or cleaving transparent samples [15].

Bessel-beams have also been considered as interesting tools for the fabrication of photonic-crystal structures [16]. In this context, the characteristic dimensions of the fabricated channels or holes are critical. For instance, in integrated optics, 2D photonic crystal structures providing novel optical functions like super-prism, negative diffraction/refraction [17] or photonic band gap [18,19] are usually composed by a block of periodically arranged holes. Typically, these holes are desired to have taper-free profiles, hundreds of nanometers in diameter and a few micrometers in depth. Despite the effectiveness of short-pulse-duration

#355963 https://doi.org/10.1364/OE.27.006996
Journal © 2019 Received 20 Dec 2018; revised 8 Feb 2019; accepted 8 Feb 2019; published 25 Feb 2019

Optics EXPRESS

Gaussian-Bessel beams for drilling high aspect ratio channels, it is quite challenging to precisely manipulate the characteristics of the fabricated holes and to access diverse aspect ratios. In our previous work [20], we demonstrated the front-surface fabrication of moderate aspect ratio micro-channels in fused silica by Gaussian–Bessel laser pulse of picosecond (ps) duration. High quality taper-free channels with excellent cylindrical shape, mean diameter of ~1.2 µm and length of ~40 µm were fabricated. However, further downscaling of the spatial characteristics of these channels is still required.

Fabricating taper-free channels (from the front surface) with aspect ratio of a few units is challenging. Highly focused Gaussian beams are not well suited to this aim, because: (i) strong absorption of the beam in the first hundred(s) of nanometers of the material may drastically limit the accessible depth, so the crater profile does not replicate the beam profile [13], and (ii) considering a radial energy relaxation profile, a Gaussian-Bessel beam is prone to reduce channel tapering with respect to Gaussian beam, and also to avoid non-uniform crater profiles observed in the literature [21]. However, it is not straightforward for a Gaussian-Bessel beam to directly fabricate channels with aspect ratio of a few units. This requires dedicated engineering of the beam. Shaping the spatial phase and/or the amplitude was shown to be effective in tailoring the intensity distribution. For instance, the side lobes of a conventional Bessel beam can be eliminated by introducing a specially designed binary phase plate in the beam path before the axicon [22]. Beam filtering at the Fourier plane of a 4f optical system with a stopper and aperture efficiently suppresses the undesired axial modulation [23]. The axial intensity profile can also be customized: by using spatial light modulators that enable to engineer the beam propagation, on-axis intensities with uniform, increasing/decreasing [24,25] or length-tunable profiles [26] have been demonstrated. In the present work, we use a simple and convenient solution – near-field filtering with an annular slit – to tailor the depth of focus (DOF) of the Gaussian-Bessel beam, and we show the interests of this technique to machine short-length microchannels on the front-surface of transparent dielectric materials.

The paper is organized as follows. First, we generate and characterize a truncated Gaussian-Bessel (TGB) beam that preserves the merit of Bessel beams and has about one quarter the DOF of the initial Gaussian-Bessel beam. To support our development, we analyze numerically the influence of the annular slit width on the spatial beam distribution. Then we use our customized TGB beam to perform single-shot ablation experiments on the front surface of a fused silica sample at different pulse energy and for the two pulse durations of 25 fs and 1 ps. The geometrical characteristics of the ablated channels are characterized by optical microscopy and scanning electron microscopy. Finally, we demonstrate that under proper processing conditions, arrays of non-through channels matching the requirements for the fabrication of photonic integrated circuits (submicron opening size, aspect ratio < 10, repeatability with high accuracy) are accessible.

2. Generation and characterization of a short-DOF beam by truncation of a Gaussian-Bessel beam

The experiment is performed with the beam line 5A (1 mJ, 100 Hz, 25 fs, linearly polarized, 800 nm) of the Ti:Sapphire ASUR laser platform (Applications des Sources Ultra-Rapides) of LP3 laboratory. The schematic of the beam shaping setup is shown in Fig. 1(a). It basically consists of an axicon (Altechna, 1-APX-2-H254-P, n = 1.45, nominal base angle = 1°) providing a first Bessel region, and a 4f demagnification optical system (with a factor of 50) made of a lens (f_1 = 500 mm) and a microscope objective (20 ×, NA = 0.4, f_2 = 10 mm, Mitutoyo NIR, working distance 20 mm) to get a second Bessel region (with half conical angle of 21.4° in air) adapted for micromachining. The setup and characteristics of the optical elements used are the same as in [20] except that here we further tailor the beam by inserting specially designed annular apertures in the beam path, just after the axicon. These annular apertures are home made by laser peeling treatment on metal-coated (600 nm thick copper

Optics EXPRESS

film) glass slides. Their geometrical characteristics are summarized in the Table 1 in Section 3. To achieve the shortest pulse duration before hitting the sample surface, the dispersion accumulated along the beam path during propagation is pre-compensated. The pulse duration is further varied by tuning the grating distance in the optical compressor. We performed experiments at the nominal pulse duration (25 fs) of the laser system and, following promising results as we demonstrated recently [20], with chirped pulses of 1 ps duration. For channel fabrication, the front surface of the dielectric sample (fused silica, Corning 7980-5F) is precisely positioned at the peak intensity point of the line focus in the second Bessel region via a motorized 3D translation stage. A synchronized mechanical shutter enables us to work in the single shot regime.

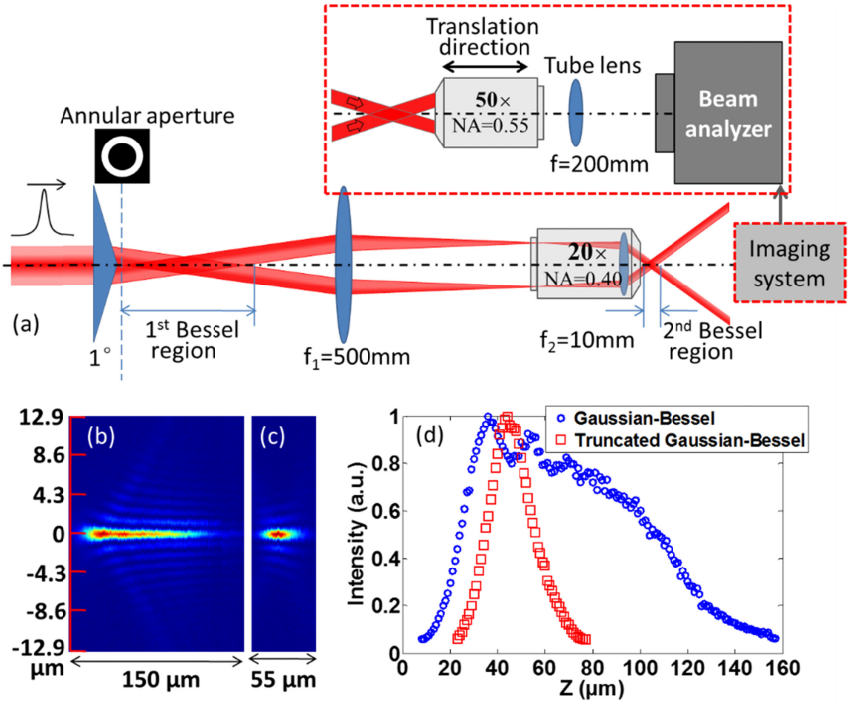

Fig. 1. (a) Schematic diagram of the experimental setup. The dashed line indicates the position where the annular aperture is inserted for truncating the initial Gaussian-Bessel beam in order to manipulate its properties in the 2nd Bessel region. All beams are characterized in air by the imaging system. The detailed arrangement of the imaging system is shown in the inset above. (b) Comparison of the propagation of the Gaussian-Bessel beam, and (c) the TGB beam resulting from annular truncation (slit width of 420 μm and mean radius of 1185 μm). (d) The normalized axial intensities of these two beams are plotted versus the optical axis using the same range of z coordinate for easy comparison.

Since the intensity distribution in the central lobe of the beam has significant impact on the material excitation and the eventual formation of the channels, we carefully characterize the intensity profiles of the generated beams in air in the second Bessel region. The beam is collinearly imaged through a 50 × objective (NA = 0.55) and a tube lens (f = 200 mm) on a beam analyzer (Gentec Beamage, with pixel size of 6.45 μm). By axially scanning and recording the transverse beam distributions along the optical axis with 1 μm step and stacking them together, the 3D intensity distribution of the beam is reconstructed. For comparison, the initial Gaussian-Bessel beam and the TGB beam are shown in Figs. 1(b) and 1(c). Note here that the horizontal direction of these two images is compressed by a factor of ~7.8 for easier demonstration. Due to manufacturing constraints, the shape of the axicon usually does not fully match the ideal conical surface. The fabrication error is especially detrimental near the

Optics EXPRESS

axicon tip apex, which leads to the typical horn-shape at the beginning of the Gaussian-Bessel beam and the intensity oscillations along the propagation axis [24,27]. The mean size of the central lobe of the beam is estimated as ~840 nm and DOF ~80 μm at full width at half maximum (FWHM).

A straightforward technique to achieve a Bessel beam with shorter DOF is to truncate the incident Gaussian beam with a circular aperture [28]. However, in view of keeping away the undesired effects from the imperfect apex of the axicon, that induce intensity modulations along the propagation axis, we additionally block the central area of the beam. To this aim, we thus place an annular aperture, with width of 420 μm and mean radius of 1185 μm to perform beam truncation just next to the axicon. The insertion energy loss of the annular slit was measured to be relatively high, approximately 86%, but this is not detrimental for the present experiments since we dispose of a large reserve of energy. The TGB beam is shown in Fig. 1(c). The size of the central lobe is slightly increased (~970 nm at FWHM), and interestingly a slight inverse tapering profile of the beam is observed. These effects come from the fact that the slit truncation causes wave diffraction. Finally, the TGB beam obtained here not only clearly shows a shorter DOF, from ~80 μm (Gaussian-Bessel beam) to ~20 μm, but also it has a smoother axial intensity profile and a better stability of beam distribution than the initial Gaussian-Bessel beam in practice. Figure 1(d) plots the normalized axial intensities of these two beams, and shows their relative axial positioning.

3. Simulation of the truncated Gaussian-Bessel beam

In this section, the propagation of the truncated beam is simulated, in order to justify our choice of the appropriate annular slit width, and to identify the limitations of this method to get the shortest uniform DOF. The simulation is performed only in the first Bessel region due to the paraxial conditions required by the scalar Fresnel diffraction theory. However, the beam propagation in the second Bessel region is closely related to the first region through the 4f system taking into account its image relay function (with a demagnification factor of 50 and 2500, respectively in transversal and axial directions).

3.1 Modeling of propagation

Free wave propagation can be described according to the Fresnel diffraction integral [29]:

$$U'(x,y)=\frac{\exp(ikZ)}{i\lambda Z}\left[U(x,y)\otimes h(x,y)\right] \tag{1}$$

$U'(x,y)$ is the complex amplitude of the field to be solved at a plane where the beam has traveled along a distance Z. $U(x,y)$ is the input field distribution at the original point of Z = 0. The symbol '⊗' stands for the convolution operator. $h(x,y)$ is the convolution kernel containing the quadratic phase term [29]:

$$h(x,y)=\exp\left[\frac{ik}{2Z}\left(x^2+y^2\right)\right] \tag{2}$$

Discretizing the two terms in Eq. (1) to $U(m,n)$ and $h(m,n)$, and making use of the convolution theorem, the above-mentioned convolution calculations can be switched to two Fourier transforms and one inverse Fourier transform (see Eq. (3)). The reason of this mathematical treatment is to improve the computing speed thanks to the fast Fourier transform (FFT) algorithm.

$$U'(m,n,Z)=\frac{\exp(ikZ)}{i\lambda Z}\times FFT^{-1}\left\{FFT\left[U(m,n)\right]\cdot FFT\left[h(m,n)\right]\right\} \tag{3}$$

Optics EXPRESS

By solving $U'(x,y)$ at successive Z planes, the 3D distribution of the diffracted beam can thus be constructed.

Experimentally, three different annular apertures were used, whose characteristics are summarized in Table 1. The parameters R, r and dw are defined in Fig. 2(a).

Table 1. Characteristics of the three different annular apertures.

No.	R (μm)	r (μm)	$\bar{r} = (R+r)/2$ (μm)	$dw = R - r$ (μm)
1	1395	975	1185	420
2	1296	1074	1185	222
3	1245	1124	1184.5	121

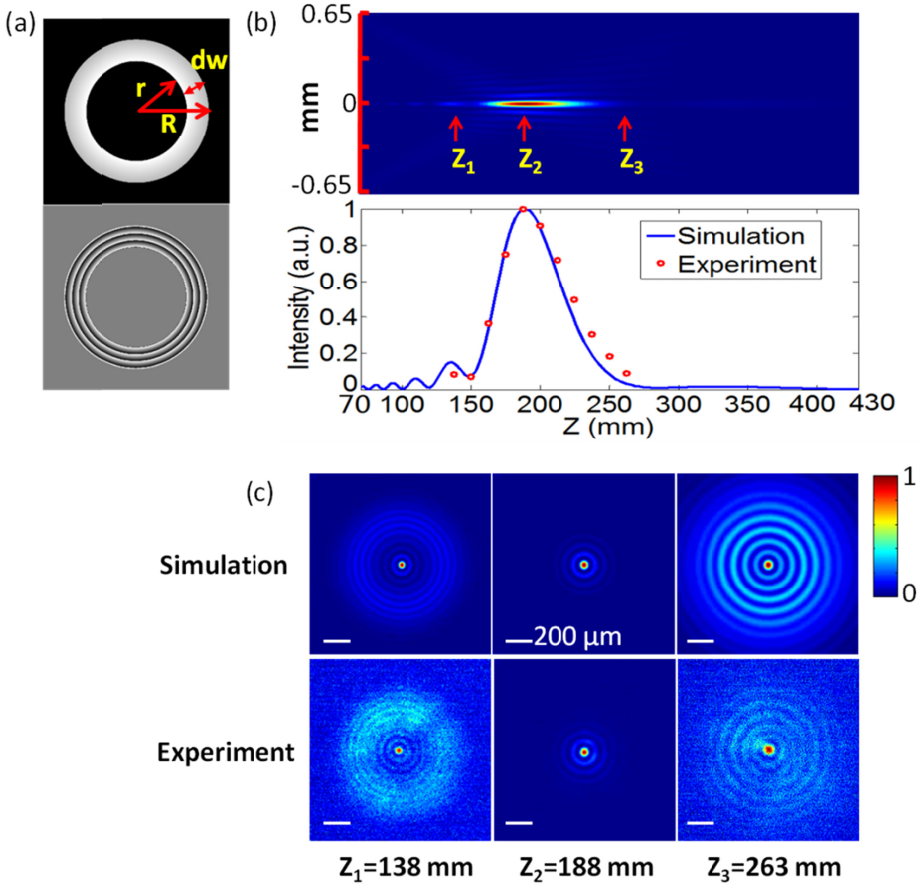

Fig. 2. Simulations of the TGB beam in the first Bessel region. (a) Top: the intensity of the transmitted wave through the annular aperture (No. 1 aperture in Table 1); Bottom: the wrapped phase of the transmitted wave. (b) Top: 2D simulation profile of the propagation of the TGB beam. The red arrows indicate the three positions presented in (c); Bottom: the axial intensity plot of the beam. (c) The transverse image of the beam at three typical axial positions in the first Bessel region, top is the simulation result; bottom is the corresponding experimental result. Each subplot has the size of 1.3 mm × 1.3 mm. The scale bar added for reference equals 200 μm for all images.

Figure 2 presents the simulation results in the case of aperture No. 1. In this example, the used input field $U(x,y)$ is visualized in Fig. 2(a). The top image depicts the intensity of the

Optics EXPRESS

initial Gaussian beam ($1/e^2$ radius equals to 2.5 mm according to the experimental condition) just after the annular truncation. The bottom image in Fig. 2(a) is the wrapped conical phase of the wave induced by the ~0.78° base angle axicon. We chose this angle value because it yields the best agreement between simulation and experimental results. It is within the claimed manufacturer uncertainty (± 0.25°) of the used axicon, which nominal base angle is 1°. The simulated profile of the beam distribution from Z = 70 mm to 430 mm is shown in the top image of Fig. 2(b). The bottom is the plot of the normalized beam axial intensity. Corresponding measurements of the beam are also carried out in the first Bessel region. Eleven slices (equally separated with steps of 12.5 mm) of the beam are recorded by the beam analyzer. The normalized intensity distribution images at three typical locations of Z = 138 mm, 188 mm, 263 mm are examined as presented in Fig. 2(c) to confirm the validity of the simulation. It appears to agree well with the experimental result. For Z_2 = 188 mm plane for example, the beam has a size of ~51 μm at FWHM in both simulation and experiment.

3.2 Optimization of the depth-of-focus

Now, we focus on the following questions: can the DOF of the TGB beam be freely manipulated by adjusting the slit width of the applied annular aperture, and what is the limitation of this method in getting the shortest DOF? One can clearly see in the simulations in Figs. 3(a)-3(c) the evolution of the beam profile as the slit width of the annular aperture decreases gradually. Note here the color figure is normalized according to the maximum intensity of each sub-image itself. The horizontal sizes of these images are 360 mm, exactly the same as Fig. 2(b) top. The initial Gaussian-Bessel beam (full beam) has a smooth but elongated axial distribution, as shown in the first subplot of Fig. 3(a). When the slit width of the applied aperture dw decreases until 620 μm, DOF of the beam decreases accordingly, but modulations occur in the beam profile. Several intensity maxima appear along the optical axis, which is not suitable for laser drilling of uniform channels. By successively decreasing dw to 420 μm, 220 μm, and 120 μm corresponding to the three apertures listed in the Table 1, a single axial intensity peak can be obtained.

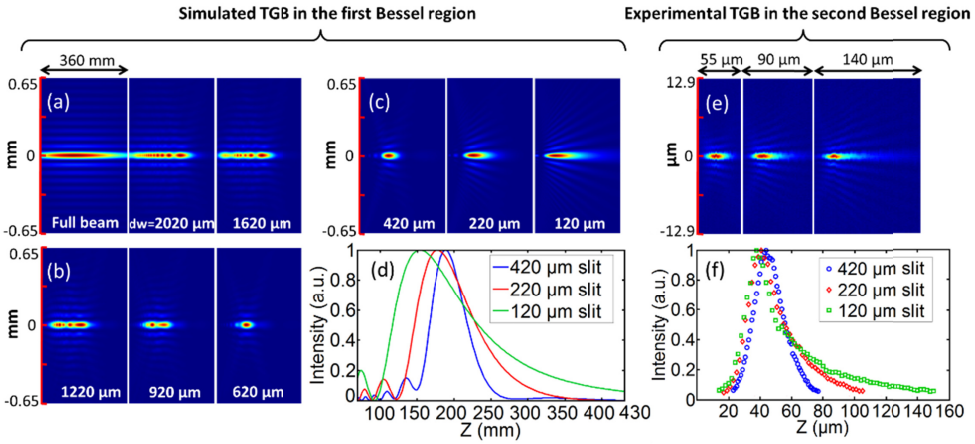

Fig. 3. Profiles of the TGB beam as a function of the slit width of the applied annular aperture. (a-c) Simulation of the 2D beam profile in the first Bessel region versus the slit width dw gradually decreasing from full beam transmission to dw = 120 μm. The mean radii of the ring aperture are all set as $\bar{r}$ = 1185 μm. (d) Normalized axial intensity curves corresponding to (c). (e) Experimental intensity distribution in the second Bessel region. Slit width dw is 420 μm, 220 μm, 120 μm in sequence, corresponding to the three subplots in (c). (f) Normalized axial intensity curves corresponding to (e).

However, the beam begins to present a divergent profile and exhibits a surprisingly increasing DOF. This illustrates the limitation of this slit truncation method in getting a

Optics EXPRESS

diffraction-free beam with very short DOF (see Fig. 3(c)). In the second Bessel region, the corresponding measurements of the beam as shown in Fig. 3(e) also confirm the inverse tapering profile. As a conclusion, we identify ~420 μm as the optimal slit width for beam truncation in view of achieving low and moderate (1-20) aspect ratio taper-free micromachining since i) the beam has a smooth axial intensity profile and keeps a small transverse size (~970 nm); ii) this arrangement preserves the diffraction-free feature of the Bessel beam on a sufficient spatial extent (~20 μm). Channel fabrication experiments in the following section are performed by using this TGB beam.

4. Machining results and discussions

4.1 Characterization of channel opening

For comparison, the experiments are performed for two pulse durations of 25 fs and 1 ps. In each case, the pulse energy was varied from 2.32 μJ to 0.28 μJ. Energy steps are set as small as 30 nJ at low energies for fine control of the channel fabrication. Each channel is processed by a single shot. Two adjacent channels are separated by 20 μm to prevent potential mutual influence.

As shown in Fig. 4, the processed channels are imaged by a 100 × optical microscope objective (Nikon, LV-UEPI-N) in both top view (reflection) and side view (transmission). When irradiating with energy much higher than the surface ablation threshold, e.g. 2.32 μJ for 25 fs pulse duration, a footprint of the typical Bessel pattern, with side rings similar to the middle image of Fig. 2(c), is engraved on the surface of the sample. For 1 ps pulse duration and same energy, less surface regions are ablated due to the smaller peak intensity of the laser pulse. As the applied energy decreases until all side rings are not intense enough for ablation, a single hole with round opening is obtained in both cases. The side views show that, in the 25 fs case, ablation is always confined in the superficial region, even when a high pulse energy is applied (ablation depth saturates at around 3 μm). For the 1 ps case, channel as long as 28 μm can be processed with the highest energy of 2.32 μJ, but ablation related to the side lobes is also visible until about 2 μm depth near the surface.

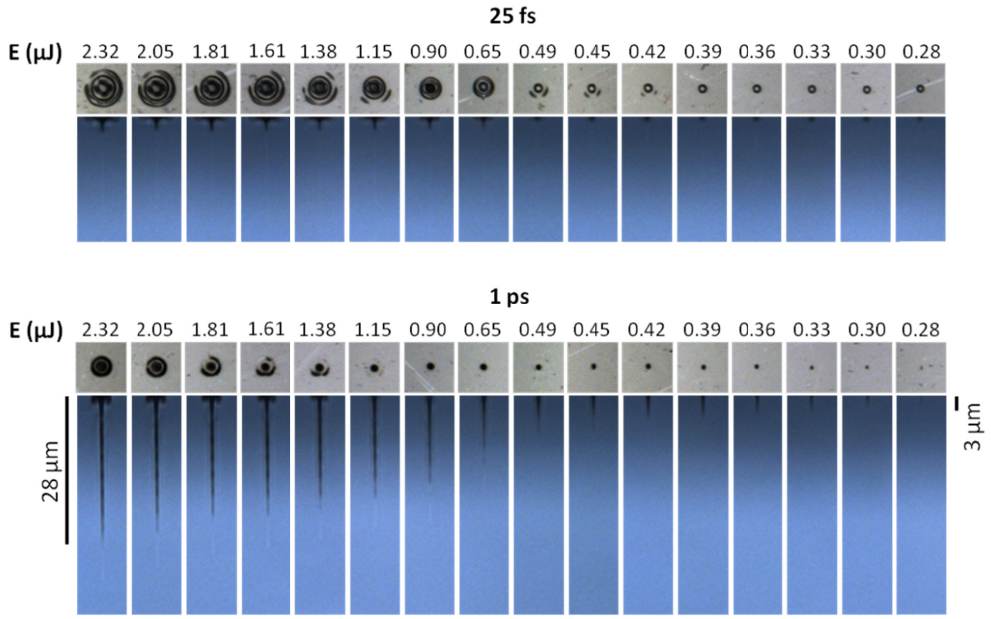

Fig. 4. Optical microscope images of the channels fabricated by 25 fs and 1 ps single-shot laser pulses. The top view (each has a size of 9.5 μm × 9.5 μm) and side view of channels are

Optics EXPRESS

presented to reveal the evolution of the modifications as a function of pulse energy. Laser beam comes from the top for all side view images.

We further characterized the surface morphologies of channels made by 25 fs and 1 ps pulses (see Fig. 5). The characterization was realized without any post-processing. The sample surface was coated with 5 nm gold film before scanning electron microscopy imaging (SEM, JEOL JSM-6390). Eight typical energies are selected in each group, which is sufficient for tracing the evolution of the surface characteristics of the channels. In addition to the top view images in Fig. 4, more details can be discerned thanks to the high resolution of SEM. It is interesting to find in the 25 fs channel group that, as the energy increases, a bubble gradually emerges in the center and eventually collapses, leaving a sunk thin film with a hole in the middle, of diameter of hundred nanometer (2.32 μJ case). This suggests that matter beneath the surface has undergone soft expansion in liquid-gas mixing phase instead of violent shocking or explosion, due to the relatively inefficient energy deposition in the material, but probably also due to a lack of longitudinal pressure release. Regarding the 1 ps group, always clear openings of the channels is observed. When the applied pulse energy is less than 0.9 μJ, a single hole without surrounding rings and with a clean morphology and surrounding area is obtained. The opening diameter becomes submicrometric for an energy below 0.45 μJ. The minimal diameter achievable here is equal to 300 nm at the lowest energy of 0.28 μJ.

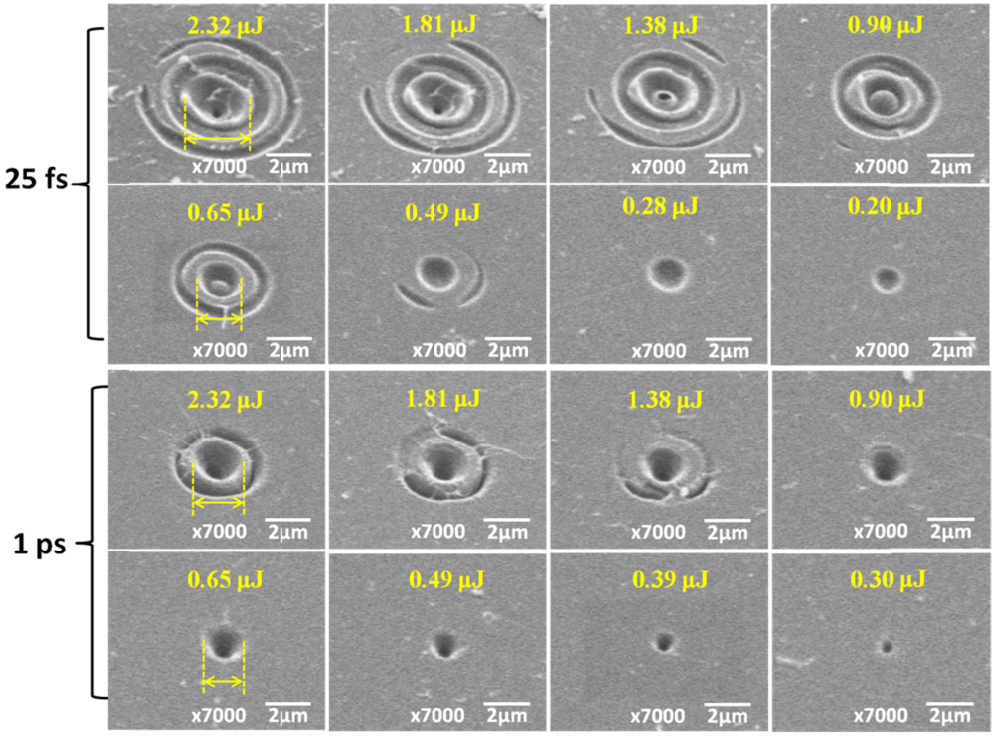

Fig. 5. Surface morphologies of the channel openings are characterized by SEM. The sample has been tilted by 40° for better imaging. The dashed line pairs indicate the measured opening diameters of the central primary holes which are analyzed in Section 4.2.

4.2 Channel aspect ratio

The characteristics of the channels can be adjusted according to the applied pulse energy. The size of the channel opening (diameter) is measured from the SEM images, and the depth of channels is extracted from the side-view microscopy images. When high energy is applied and high order rings exist at the opening surface, we define the channel diameter as only the

Optics EXPRESS

primary central hole, counting the ridge as the edge of hole (see yellow arrows in Fig. 5). The reason for this choice is that it enables: (i) to have the same definition whatever the pulse energy and for both pulse durations, therefore enabling relevant comparisons; and (ii) to follow its evolution upon decrease of energy, when surrounding rings progressively disappear. Note that, for the 25 fs, 2.32 µJ case, this definition does not account for the very thin crater in the center. By the way, such regime could be very interesting to drill nanochannels, but the counterpart is that that surface morphology is not clean around the channel. In the present work, we thus focus on low-energy regime. Regarding the crater depth, as it is not constant over the transverse profile at the surface in the femtosecond high energy regime, we use the maximum channel depth as a definition.

Now, the evolutions of the size of the channel opening (diameter) and the channel length (depth) are plotted as a function of pulse energy and for the two pulse durations, as shown in Figs. 6(a) and 6(b).

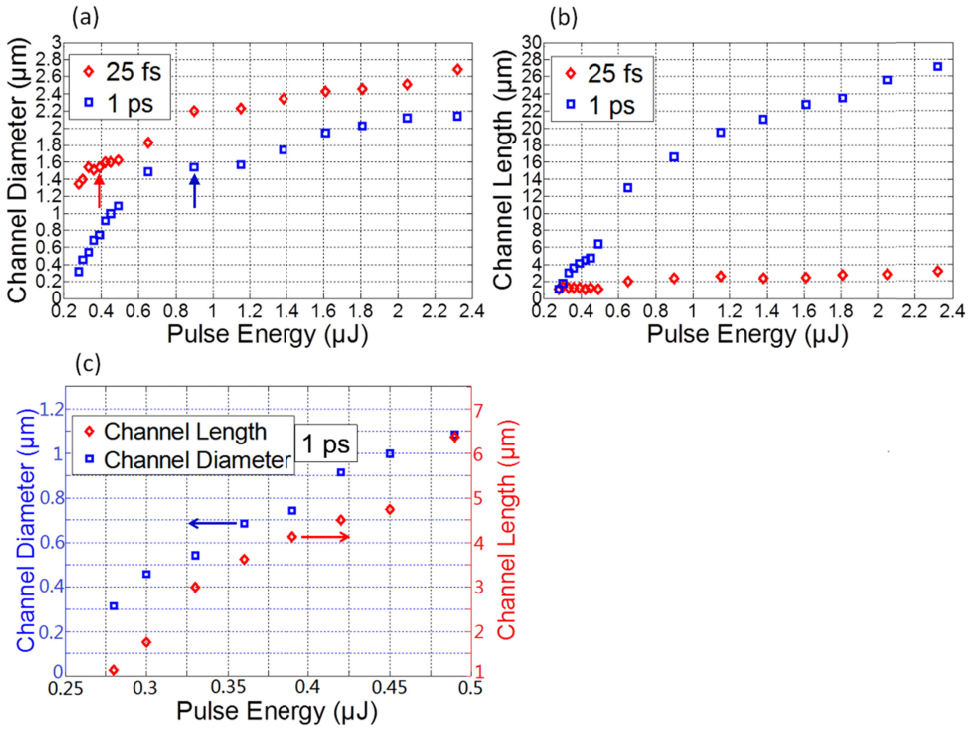

Fig. 6. Dependence of channel diameter (a) and channel length (b) as a function of the applied pulse energy and for the two pulse durations of 25 fs and 1 ps. (c) A zoomed graph of the most interesting range (1 ps case, E < 0.5 µJ) including channel diameter and length.

The two arrows in Fig. 6(a) indicate the threshold energy at both pulse durations below which a single hole could be obtained, without high order rings on surface. Regarding the length of the channels (Fig. 6(b)), picosecond pulses are clearly more efficient for deep ablation. We observe a strong limitation in the laser processed range that can be accessed when 25 fs pulses are used in comparison to 1 ps pulses. Several works have contributed to the subject of Bessel beam propagation in nonlinear media [30–33]. It can be inferred that ps pulses undergo less significant nonlinearities compared to fs pulses. In particular, due to the inherent facility of intense ultrashort pulses to create a free electron plasma through nonlinear absorption, strong defocusing effects take place causing scattering of the TGB beam away from the energy deposition axis during its propagation in the bulk of the dielectric sample [33]. In our cases, TGB beam with ps pulse duration could maintain its shape in a more

Optics EXPRESS

stationary way and waste less energy than fs pulses before the laser pulse deposits its energy in the material in the intense central core volume. Note that it has been shown that Bessel beams with low cone angle are more vulnerable to nonlinearities [32]. Increasing the latter could be a route for reducing the limitation observed with ultrashort (25 fs) pulses. Finally, Bhuyan et al. [34] reported that, at low cone angle of 7° in fused silica, chirping laser pulses from fs to ps regime can be an effective strategy to fight against the poor stability of nonlinear Bessel beams, and to improve the energy deposition efficiency for bulk material modification, which is in support of our experimental result. Similar conclusions were also obtained by Garzillo et al. [35] in a different glassy material (BK7).

The most interesting range for short-length channel processing (1 ps case, $E < 0.5$ µJ) is plotted in Fig. 6(c), regrouping the evolution of channel diameter and length. It clearly shows that small aspect ratios, in the range of ~5, with sub-micrometric opening diameter, can be obtained using 1 ps pulses of low energy. The shortest channel length could approach the level of one micron with the lowest energy applied here of 0.28 µJ. Moreover, comparing the in-depth transverse profiles at different depths (using for example the case of energy of 0.36 µJ in Fig. 4), we observe that the diameter of the channel does not vary significantly, in agreement with previous experiments and dedicated analysis [20]. Using post-mortem polishing procedure, it is possible to further decrease the aspect ratio by removing calibrated thicknesses of matter at the sample surface, as also demonstrated in [20]. This way, taper-free holes with even smaller aspect ratio (in the range 1-5) and diameter opening below the upper wavelength of visible range are reachable when small-energy 1 ps pulses are used.

4.3 Processing of matrices of channels

Finally, to highlight the interest of the tailored short TGB laser pulses and their flexibility for single step direct writing of two-dimensional photonic crystal structures, we fabricated square matrices of 10 × 10 channels with spatial pitch of respectively 5 µm, 3 µm, and 1.5 µm (see Figs. 7(a)-7(c)). They are processed sequentially by using single pulses of 1 ps duration and 0.36 µJ energy, corresponding to channel dimensions of 680 nm in diameter and 3.6 µm in length (see Fig. 6(c), which is used as a look-up table). We chose these parameters on the basis of the results shown above.

The obtained matrices show densely-packed channels, that are regular in terms of morphology, with little residual side effects (such as bump, melted zone, etc.) around the opening of every channel. Indeed, the surrounding affected zone is << 100 nm (much below the inter-channel spacing, even in the 1.5 µm case). Fluctuations in the separation of channels are observed, which is mainly attributed to the limitations of the translation stage. Note the pollutants on surface become more apparent when smaller separations are applied due to the increasing density of residues. Air-blowing or liquid immersion strategies can be considered during the laser ablation for improvement in future works.

To confirm the void nature of the channels in bulk, the sample surface is repeatedly polished, metalized and characterized by SEM. As an example, we show in Fig. 7(d) the sample surface of the 5 µm pitch matrix when 0.5 µm material thickness is removed by polishing away. The filling of the channels (see the white spots in SEM) is attributed to post processing polishing substances. Indeed, these fillings have been identified as CeO_2 from Energy Dispersive Spectroscopy (EDS) coming from 2.5 µm CeO_2 powder used for sample polishing, see Fig. 7(e). The dark spots in Si image (Fig. 7(f)) explicitly indicate the lack of a-SiO_2, thus confirming the void formed there.

Optics EXPRESS

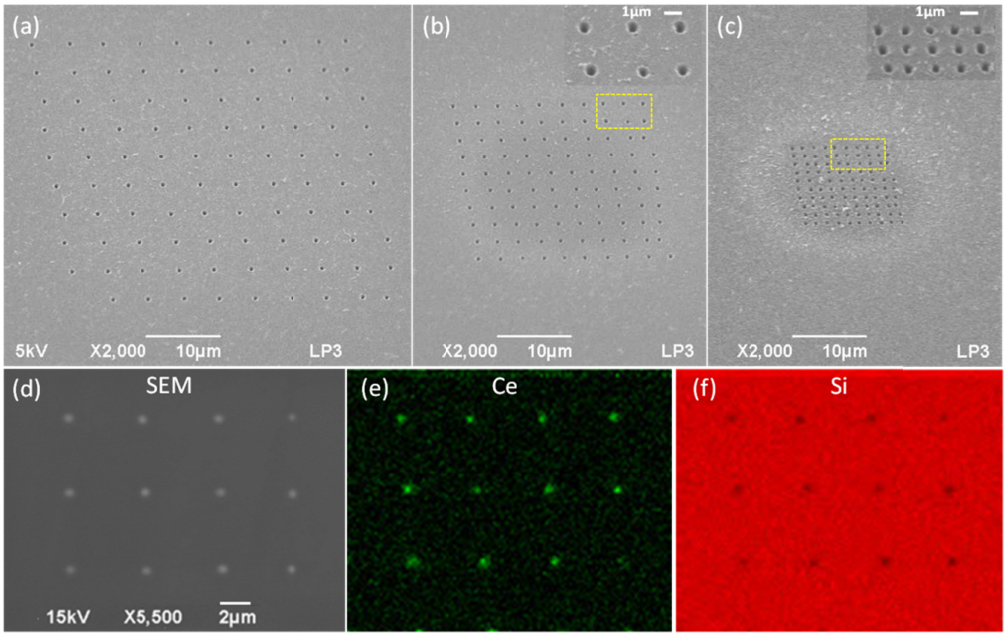

Fig. 7. 10 × 10 channel arrays, with periods of: (a) 5 μm, (b) 3 μm, and (c) 1.5 μm, fabricated by the TGB beam with 1 ps pulse duration and 0.36 μJ pulse energy. As indicated by the yellow dashed boxes in (b) and (c), the insets show zooms in the upper-right corner of the matrix for better resolution. (d,e,f): elemental analysis by EDS on the polished sample surface.

5. Conclusions

Annular aperture truncated Gaussian-Bessel beam technique has been developed for direct processing of channels with moderate to small aspect ratio (from ~12 to ~3), controllable via the energy, pulse duration and truncation factor. Truncation conditions are investigated through both simulation and experimental studies to reveal the range of applicability of this method in tailoring the depth-of-field of the Gaussian-Bessel beam (reduction by a factor 4). For channel processing, 1 ps pulse duration has been found to be more favorable than 25 fs. We demonstrate that sub-micron size channels (down to 300 nm diameter) with variable length in the micrometric range and negligible side effects can be processed when single 1 ps pulses are applied with pulse energy less than 0.45 μJ. Finally, 10 × 10 channel arrays with "lattice constant" as small as 1.5 μm are fabricated, with a good opening quality (without the need of post-polishing of the surface) and an aspect ratio of ~5 which can be downscaled by using additional post-polishing procedure [20] or upscaled by varying the laser operating conditions. We anticipate that the high flexibility offered by the irradiation from the front side (complementary to other works, e.g. [16].) contributes to open broader perspectives of application of such nanofabrication technique, in view of direct laser writing of photonic-crystal structures in various materials.

Funding

China Scholarship Council (CSC), National Key Research and Development Program of China (Grant No.2018YFB11074), National Natural Science Foundation of Zhejiang (No.LY14F050002), Agence Nationale de la Recherche (project Smart-Lasir 11BS09026), European Community, Ministry of Research and High Education, Region Provence-Alpes-Côte d'Azur, Department of Bouches-du-Rhône, City of Marseille, CNRS, Aix-Marseille University.

Optics EXPRESS

Acknowledgments

We thank D. Grojo, R. Clady, L. Charmasson and J. L. Bellemain for helpful discussions and technical assistance.

References

1. J. Durnin, J. Miceli, Jr., and J. H. Eberly, "Diffraction-free beams," Phys. Rev. Lett. **58**(15), 1499–1501 (1987).
2. R. P. MacDonald, S. A. Boothroyd, T. Okamoto, J. Chrostowski, and B. A. Syrett, "Interboard optical data distribution by Bessel beam shadowing," Opt. Commun. **122**(4-6), 169–177 (1996).
3. N. Blow, "Cell imaging: New ways to see a smaller world," Nature **456**(7223), 825–828 (2008).
4. C. L. Arnold, S. Akturk, A. Mysyrowicz, V. Jukna, A. Couairon, T. Itina, R. Stoian, C. Xie, J. M. Dudley, F. Courvoisier, S. Bonanomi, O. Jedrkiewicz, and P. Di Trapani, "Nonlinear Bessel vortex beams for applications," J. Phys. At. Mol. Opt. Phys. **48**(9), 94006–94016 (2015).
5. D. McGloin and K. Dholakia, "Bessel beams: diffraction in a new light," Contemp. Phys. **46**(1), 15–28 (2005).
6. G. Zhang, R. Stoian, W. Zhao, and G. Cheng, "Femtosecond laser Bessel beam welding of transparent to non-transparent materials with large focal-position tolerant zone," Opt. Express **26**(2), 917–926 (2018).
7. M. K. Bhuyan, F. Courvoisier, P. A. Lacourt, M. Jacquot, R. Salut, L. Furfaro, and J. M. Dudley, "High aspect ratio nanochannel machining using single shot femtosecond Bessel beams," Appl. Phys. Lett. **97**(8), 081102 (2010).
8. M. Duocastella and C. B. Arnold, "Bessel and annular beams for materials processing," Laser Photonics Rev. **6**(5), 607–621 (2012).
9. R. Stoian, M. K. Bhuyan, G. Zhang, G. Cheng, R. Meyer, and F. Courvoisier, "Ultrafast Bessel beams: advanced tools for laser materials processing," Adv. Opt. Technol. **7**(3), 165–174 (2018).
10. F. Courvoisier, R. Stoian, and A. Couairon, "Ultrafast laser micro- and nano-processing with nondiffracting and curved beams," Opt. Laser Technol. **80**, 125–137 (2016).
11. E. Toratani, M. Kamata, and M. Obara, "Self-fabrication of void array in fused silica by femtosecond laser processing," Appl. Phys. Lett. **87**(17), 171103 (2005).
12. M. K. Bhuyan, F. Courvoisier, P.-A. Lacourt, M. Jacquot, L. Furfaro, M. J. Withford, and J. M. Dudley, "High aspect ratio taper-free microchannel fabrication using femtosecond Bessel beams," Opt. Express **18**(2), 566–574 (2010).
13. O. Utéza, N. Sanner, B. Chimier, A. Brocas, N. Varkentina, M. Sentis, P. Lassonde, F. Légaré, and J. C. Kieffer, "Control of material removal of fused silica with single pulses of few optical cycles to sub-picosecond duration," Appl. Phys., A Mater. Sci. Process. **105**(1), 131–141 (2011).
14. S. Mitra, M. Chanal, R. Clady, A. Mouskeftaras, and D. Grojo, "Millijoule femtosecond micro-Bessel beams for ultra-high aspect ratio machining," Appl. Opt. **54**(24), 7358–7365 (2015).
15. L. Rapp, R. Meyer, L. Furfaro, C. Billet, R. Giust, and F. Courvoisier, "High speed cleaving of crystals with ultrafast Bessel beams," Opt. Express **25**(8), 9312–9317 (2017).
16. F. Courvoisier, J. Zhang, M. K. Bhuyan, M. Jacquot, and J. M. Dudley, "Applications of femtosecond Bessel beams to laser ablation," Appl. Phys., A Mater. Sci. Process. **112**(1), 29–34 (2013).
17. B. Momeni, J. Huang, M. Soltani, M. Askari, S. Mohammadi, M. Rakhshandehroo, and A. Adibi, "Compact wavelength demultiplexing using focusing negative index photonic crystal superprisms," Opt. Express **14**(6), 2413–2422 (2006).
18. M. Roussey, M.-P. Bernal, N. Courjal, and F. I. Baida, "Experimental and theoretical characterization of a lithium niobate photonic crystal," Appl. Phys. Lett. **87**(24), 241101 (2005).
19. G. W. Burr, S. Diziain, and M.-P. Bernal, "The impact of finite-depth cylindrical and conical holes in lithium niobate photonic crystals," Opt. Express **16**(9), 6302–6316 (2008).
20. X. Liu, N. Sanner, M. Sentis, R. Stoian, W. Zhao, G. Cheng, and O. Utéza, "Front-surface fabrication of moderate aspect ratio micro-channels in fused silica by single picosecond Gaussian-Bessel laser pulse," Appl. Phys., A Mater. Sci. Process. **124**(2), 206 (2018).
21. N. Götte, T. Winkler, T. Meinl, T. Kusserow, B. Zielinski, C. Sarpe, A. Senftleben, H. Hillmer, and T. Baumert, "Temporal Airy pulses for controlled high aspect ratio nanomachining of dielectrics," Optica **3**(4), 389–395 (2016).
22. F. He, J. Yu, Y. Tan, W. Chu, C. Zhou, Y. Cheng, and K. Sugioka, "Tailoring femtosecond 1.5-μm Bessel beams for manufacturing high-aspect-ratio through-silicon vias," Sci. Rep. **7**(1), 40785 (2017).
23. M. K. Bhuyan, P. K. Velpula, M. Somayaji, J. P. Colombier, and R. Stoian, "3D Nano-fabrication using controlled Bessel-glass interactions in ultrafast modes," J. Laser Micro Nanoen. **12**, 274–280 (2017).
24. T. Cizmár and K. Dholakia, "Tunable Bessel light modes: engineering the axial propagation," Opt. Express **17**(18), 15558–15570 (2009).
25. I. Ouadghiri-Idrissi, R. Giust, L. Froehly, M. Jacquot, L. Furfaro, J. M. Dudley, and F. Courvoisier, "Arbitrary shaping of on-axis amplitude of femtosecond Bessel beams with a single phase-only spatial light modulator," Opt. Express **24**(11), 11495–11504 (2016).
26. Z. Yao, L. Jiang, X. Li, A. Wang, Z. Wang, M. Li, and Y. Lu, "Non-diffraction-length, tunable, Bessel-like beams generation by spatially shaping a femtosecond laser beam for high-aspect-ratio micro-hole drilling," Opt. Express **26**(17), 21960–21968 (2018).

Optics EXPRESS

27. J. Dudutis, P. GeČys, and G. RaČiukaitis, "Non-ideal axicon-generated Bessel beam application for intra-volume glass modification," Opt. Express **24**(25), 28433–28443 (2016).
28. M. Cywiak, D. Cywiak, and E. Yáñez, "Finite Gaussian wavelet superposition and Fresnel diffraction integral for calculating the propagation of truncated, non-diffracting and accelerating beams," Opt. Commun. **405**, 132–142 (2017).
29. J. W. Goodman, *Introduction to Fourier optics* (McGraw-Hill, 2005).
30. P. Polesana, A. Couairon, D. Faccio, A. Parola, M. A. Porras, A. Dubietis, A. Piskarskas, and P. Di Trapani, "Observation of conical waves in focusing, dispersive, and dissipative Kerr media," Phys. Rev. Lett. **99**(22), 223902 (2007).
31. M. A. Porras, C. Ruiz-Jiménez, and J. C. Losada, "Underlying conservation and stability laws in nonlinear propagation of axicon-generated Bessel beams," Phys. Rev. A **92**(6), 063826 (2015).
32. P. Polesana, M. Franco, A. Couairon, D. Faccio, and P. Di Trapani, "Filamentation in Kerr media from pulsed Bessel beams," Phys. Rev. A **77**(4), 043814 (2008).
33. P. K. Velpula, M. K. Bhuyan, F. Courvoisier, H. Zhang, J. P. Colombier, and R. Stoian, "Spatio-temporal dynamics in nondiffractive Bessel ultrafast laser nanoscale volume structuring," Laser Photonics Rev. **10**(2), 230–244 (2016).
34. M. K. Bhuyan, P. K. Velpula, J. P. Colombier, T. Olivier, N. Faure, and R. Stoian, "Single-shot high aspect ratio bulk nanostructuring of fused silica using chirp-controlled ultrafast laser Bessel beams," Appl. Phys. Lett. **104**(2), 021107 (2014).
35. V. Garzillo, V. Jukna, A. Couairon, R. Grigutis, P. Di Trapani, and O. Jedrkiewicz, "Optimization of laser energy deposition for single-shot high aspect-ratio microstructuring of thick BK7 glass," J. Appl. Phys. **120**(1), 013102 (2016).